LETTER

Methane storage in flexible metal–organic frameworks with intrinsic thermal management

Jarad A. Mason[1], Julia Oktawiec[1], Mercedes K. Taylor[1], Matthew R. Hudson[2], Julien Rodriguez[3], Jonathan E. Bachman[1], Miguel I. Gonzalez[1], Antonio Cervellino[4], Antonietta Guagliardi[5], Craig M. Brown[2,6], Philip L. Llewellyn[3], Norberto Masciocchi[7] & Jeffrey R. Long[1]

As a cleaner, cheaper, and more globally evenly distributed fuel, natural gas has considerable environmental, economic, and political advantages over petroleum as a source of energy for the transportation sector[1,2]. Despite these benefits, its low volumetric energy density at ambient temperature and pressure presents substantial challenges, particularly for light-duty vehicles with little space available for on-board fuel storage[3]. Adsorbed natural gas systems have the potential to store high densities of methane (CH_4, the principal component of natural gas) within a porous material at ambient temperature and moderate pressures[4]. Although activated carbons, zeolites, and metal–organic frameworks have been investigated extensively for CH_4 storage[5–8], there are practical challenges involved in designing systems with high capacities and in managing the thermal fluctuations associated with adsorbing and desorbing gas from the adsorbent. Here, we use a reversible phase transition in a metal–organic framework to maximize the deliverable capacity of CH_4 while also providing internal heat management during adsorption and desorption. In particular, the flexible compounds Fe(bdp) and Co(bdp) ($bdp^{2-} = 1,4$-benzenedipyrazolate) are shown to undergo a structural phase transition in response to specific CH_4 pressures, resulting in adsorption and desorption isotherms that feature a sharp 'step'. Such behaviour enables greater storage capacities than have been achieved for classical adsorbents[9], while also reducing the amount of heat released during adsorption and the impact of cooling during desorption. The pressure and energy associated with the phase transition can be tuned either chemically or by application of mechanical pressure.

The driving range of an adsorbed natural gas (ANG) vehicle is determined primarily by the volumetric usable CH_4 capacity of the adsorbent, which is defined as the difference between the amount of CH_4 adsorbed at the target storage pressure (generally 35–65 bar) and the amount that is still adsorbed at the lowest desorption pressure (generally 5.8 bar)[8–10]. With few exceptions[11], adsorbents that have been investigated in the context of natural gas storage exhibit classical Langmuir-type adsorption isotherms, where the amount of CH_4 adsorbed increases continuously, but at a decreasing rate, as the pressure is raised (Fig. 1a). Consequently, it has proved difficult to develop adsorbents with the higher usable capacities needed for a commercially viable ANG storage system[9]. In pursuit of a new strategy for boosting usable capacity, we endeavoured to design an adsorbent with an 'S-shaped' or 'stepped' CH_4 adsorption isotherm, where the amount of CH_4 adsorbed would be small at low pressures but rise sharply just before the pressure reaches the desired storage pressure (Fig. 1b). Stepped isotherms have been observed for many flexible metal–organic frameworks that exhibit 'gate-opening' behaviour,

whereby a non-porous structure expands to a porous structure after a certain threshold gas pressure is reached, but none of these materials have exhibited characteristics beneficial for CH_4 storage applications[12–16]. If, however, a responsive adsorbent could be designed to expand to store a high density of CH_4 at 35–65 bar, and to collapse to push out all adsorbed CH_4 at a pressure near 5.8 bar, then it should be possible to reach higher usable capacities than have been realized for classical adsorbents.

The metal–organic framework Co(bdp) was selected as a potential responsive adsorbent for methane storage, owing to its large internal surface area and its previously demonstrated high degree of flexibility[17]. In its solvated form, this framework features one-dimensional chains of tetrahedral Co^{2+} cations bridged by μ^2-pyrazolates to form a structure with square channels with edge lengths of 13 Å. The N_2 adsorption isotherm of the evacuated framework at 77 K exhibits five distinct steps, which have been attributed to four structural transitions as the framework
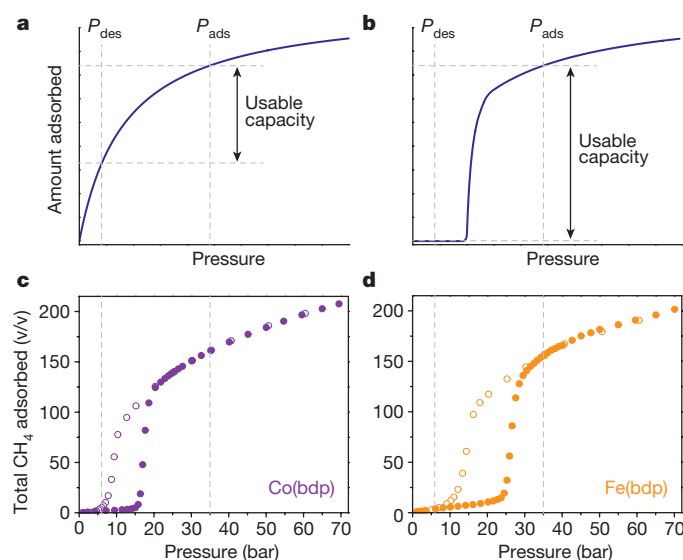

Figure 1 | High-pressure CH_4 adsorption isotherms. a, b, The usable capacity is compared for an idealized adsorbent exhibiting a classical Langmuir-type adsorption isotherm (**a**) and an 'S-shaped' or 'stepped' adsorption isotherm (**b**), with the minimum desorption pressure P_{des} and the maximum adsorption pressure P_{ads} indicated by the vertical dashed grey lines. **c, d**, Total CH_4 adsorption isotherms for Co(bdp) (**c**) and Fe(bdp) (**d**) at 25 °C. Here $P_{des} = 5.8$ bar and $P_{ads} = 35$ bar are indicated by dashed grey lines. Filled circles represent adsorption; open circles represent desorption.

[1]Department of Chemistry, University of California, Berkeley, California 94720, USA. [2]Center for Neutron Research, National Institute of Standards and Technology, Gaithersburg, Maryland 20899, USA. [3]Aix-Marseille University, CNRS Laboratoire MADIREL (UMR 7246), Centre de Saint Jérôme, 13397 Marseille Cedex 20, France. [4]Laboratory for Synchrotron Radiation – Condensed Matter, Swiss Light Source, Paul Scherrer Institute, CH-5232 Villigen, Switzerland. [5]Istituto di Cristallografia, Consiglio Nazionale delle Ricerche, and To.Sca.Lab., via Valleggio 11, 22100 Como, Italy. [6]Chemical and Biomolecular Engineering, University of Delaware, Newark, Delaware 19716, USA. [7]Dipartimento di Scienza e Alta Tecnologia, Università dell'Insubria, and To.Sca.Lab, via Valleggio 11, 22100 Como, Italy.
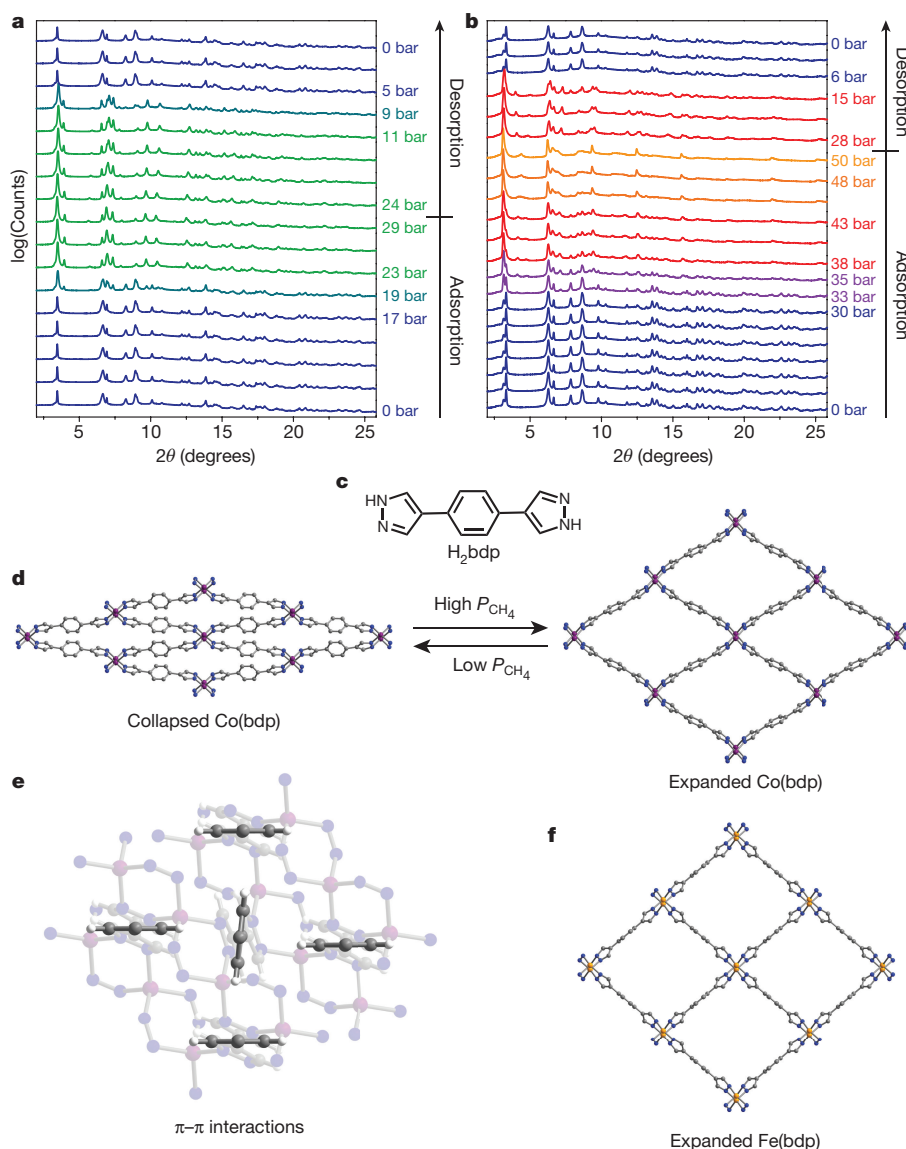
Figure 2 | Powder X-ray diffraction and solid-state structures.
a, **b**, Powder X-ray diffraction patterns (2θ is the diffraction angle) are
shown for Co(bdp) (**a**) and Fe(bdp) (**b**) at 25 °C and variable CH_4 pressures
(as indicated), with X-ray wavelengths of 0.75009 Å and 0.72768 Å,
respectively. For Co(bdp), the blue and green patterns correspond to the
collapsed and expanded phases, respectively, with teal indicating patterns in
which both phases are present during the transition between collapsed and
expanded. For Fe(bdp), the blue and red patterns correspond to the
collapsed and 40-bar expanded phases, respectively, with purple indicating
patterns in which both phases are present during the transition from

collapsed to 40-bar expanded; orange patterns correspond to the 50-bar
expanded phase. **c**, **d**, The bridging ligand precursor H_2bdp (**c**) along with
the crystal structures (**d**) of the collapsed (0 bar, 'low P_{CH_4}') and CH_4-
expanded (30 bar, 'high P_{CH_4}') phases of Co(bdp). **e**, Each benzene ring in the
collapsed phase of Co(bdp) has four edge-to-face π–π interactions with
neighbouring benzene rings. **f**, Crystal structure of the CH_4-expanded
(40 bar) phase of Fe(bdp). In **d**–**f**, Purple, orange, grey, blue, and white
spheres represent Co, Fe, C, N, and H atoms, respectively; some H atoms are
omitted for clarity.

progresses from a collapsed phase with minimal porosity to a maximally
expanded phase with a Langmuir surface area of 2,911 $m^2\,g^{-1}$ (ref. 18).

To investigate the ANG storage potential of Co(bdp), a high-pressure
CH_4 adsorption isotherm was measured at 25 °C (Fig. 1c). There is
minimal CH_4 uptake at low pressures and a sharp step in the adsorp-
tion isotherm at 16 bar. Although there is hysteresis in the desorption
isotherm, the hysteresis loop is closed by 7 bar, such that there is less
than 0.2 mmol g^{-1} of CH_4 adsorbed at pressures below 5.8 bar. The step
in the CH_4 isotherm is fully reproducible over at least 100 adsorption–
desorption cycles (Extended Data Fig. 1), and can be attributed to a
reversible structural phase transition between a collapsed, non-porous
framework and an expanded, porous framework at transition pressures
that are ideal for ANG storage.

To determine the specific structural changes responsible for the
stepped CH_4 adsorption isotherm of Co(bdp), *in situ* powder X-ray

diffraction experiments were performed under various pressures of
CH_4 at 25 °C. Under vacuum, only one crystalline phase is observed
in the diffraction pattern, consistent with the complete conversion of
Co(bdp) to a collapsed phase upon desolvation. From 17 bar to 23 bar,
there are substantial changes to both the positions and intensities of
the diffraction peaks, as peaks corresponding to the collapsed phase
decrease in intensity and peaks corresponding to a new expanded phase
increase in intensity (Fig. 2a). During desorption, this expanded phase is
fully converted back to the collapsed phase between 10 bar and 5 bar.

Owing to the anisotropic peak widths and complex peak shapes that
result from paracrystallinity effects[19], analysis of the powder diffraction
data is not trivial, but *ab initio* structure solutions followed by Rietveld
refinements (Extended Data Fig. 7) were successfully performed using
the diffraction data at 0 bar and 30 bar to provide crystal structures of
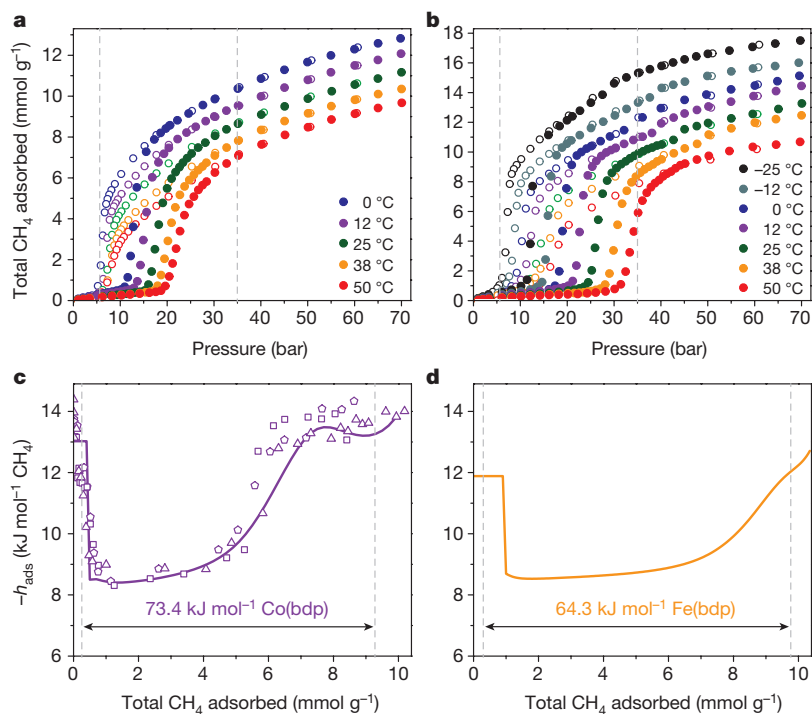the collapsed and expanded phases of Co(bdp) (Fig. 2d). As discussed

Figure 3 | Variable-temperature equilibrium isotherms and differential enthalpies. a, b, Total CH$_4$ adsorption isotherms at various temperatures for Co(bdp) (**a**) and Fe(bdp) (**b**), where a minimum desorption pressure of 5.8 bar and a maximum adsorption pressure of 35 bar are indicated by dashed grey lines. Filled circles represent adsorption; open circles represent desorption. **c**, Differential enthalpies of CH$_4$ adsorption (h_{ads}) for Co(bdp), as determined from variable-temperature adsorption isotherms (purple line) and three separate microcalorimetry experiments (open symbols). **d**, Differential enthalpies of CH$_4$ adsorption (h_{ads}) for Fe(bdp), as determined from variable-temperature adsorption isotherms. Dashed grey lines in **c** and **d** indicate the amount of CH$_4$ adsorbed at 5.8 bar and 35 bar.

in the Supplementary Information and shown in Extended Data Fig. 8, paracrystallinity arises from highly correlated shifts of the positions of Co-pyrazolate chains in the crystallographic a–b plane, whereby neighbouring chains exhibit average displacements of approximately 0.5 Å from their average periodic positions. Importantly, this minor systematic disordering has no effect on the accuracy of the average crystal structures or the calculated crystallographic densities of each phase. Additionally, a substantial diffuse-scattering component is present in the experimental diffraction patterns, particularly at high CH$_4$ loadings. Although most of the diffuse scattering can be attributed to the thick-walled quartz glass capillaries used as sample holders in the diffraction experiments at high CH$_4$ pressures (Supplementary Fig. 11), there may also be some diffuse scattering that is intrinsic to Co(bdp), which could arise from minor local disorder or from scattering by adsorbed CH$_4$ molecules.

Even though the density of the collapsed phase (1.50 g cm^{-3}) is nearly double that of the expanded phase (0.77 g cm^{-3}), the Co^{2+} ions adopt a similar pseudotetrahedral geometry in both structures. During the phase transition, the angles between the planes of the pyrazolate rings and the Co–N bonds decrease as the framework expands (Extended Data Fig. 6). In addition, the central benzene ring of the bdp^{2-} ligand twists out of the plane of the two pyrazolates by 25° in the collapsed structure, resulting in edge-to-face π–π interactions with four neighbouring benzene rings that probably provide most of the thermodynamic driving force for the collapse of Co(bdp) at low pressures (Fig. 2e)[20]. These close contacts between neighbouring bdp^{2-} ligands lead to no accessible porosity, and thus no CH$_4$ adsorption, in the collapsed phase.

The usable CH$_4$ capacity of Co(bdp) at 25 °C is 155 cm^3 STP cm^{-3} (v/v) for adsorption at 35 bar and 197 v/v for adsorption at 65 bar, which are the highest values of usable CH$_4$ capacity reported so far for any adsorbent under these conditions. A recent computational analysis of a database containing over 650,000 classical adsorbents predicted a theoretical-maximum 65-bar usable capacity of 196 v/v (ref. 9); however,

all adsorbents in this large-scale computational screening were rigid, and the potential utility of flexible adsorbents for CH$_4$ storage was not considered. The Co(bdp) usable capacities reported here are a result of the transition from the expanded to the collapsed phase leading to near complete CH$_4$ desorption by 5.8 bar. For comparison, the highest previously measured 35-bar and 65-bar usable capacities for any adsorbent are 143 v/v and 189 v/v, respectively[7,8,21]. Both of these Cu$_2$ paddlewheel-based frameworks have high densities of CH$_4$ adsorption sites with a near-optimal (for maximizing the usable CH$_4$ capacity for ambient temperature adsorption at pressures between 35 bar and 65 bar) binding enthalpy of −15 kJ mol^{-1} to −17 kJ mol^{-1}, but display Langmuir-type adsorption isotherms that leave a substantial amount of unusable CH$_4$ adsorbed at 5.8 bar.

One major, and often overlooked, challenge in developing adsorbents for natural gas storage, or indeed for any gas storage application, involves managing the exothermic heat of adsorption and endothermic heat of desorption, both of which reduce the usable capacity of an adsorbent. These heat effects can be substantial, with temperature changes of as much as 80 °C observed during testing of prototype activated carbon-based ANG systems, and result in large reductions in the usable CH$_4$ capacity[22,23]. On-board thermal-management systems are essential to minimizing the negative impacts of the heats of sorption, but these engineering controls take up already limited space on a vehicle and add considerable cost and complexity[24].

Responsive adsorbents, such as Co(bdp), offer the possibility of managing heat intrinsically within a material, rather than through an external system, by using the enthalpy change of a phase transition to partially, or perhaps even fully, offset the heats of sorption. For Co(bdp), the expansion of the framework during adsorption is endothermic, because energy is needed to overcome the greater thermodynamic stability of the collapsed phase. As a result, some of the enthalpy of CH$_4$ adsorption should go towards providing the heat needed for
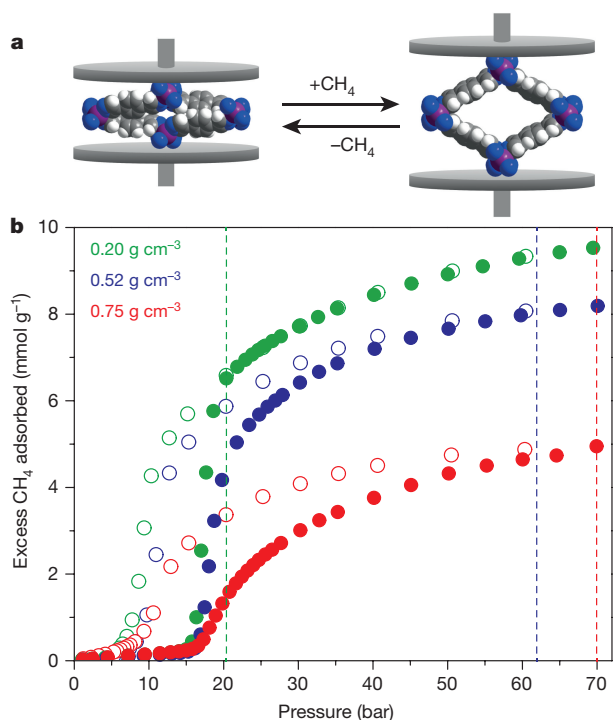
Figure 4 | Effect of mechanical pressure on CH$_4$ storage in Co(bdp).
a, Space-filling models of collapsed (left) and CH$_4$-expanded (right) Co(bdp); purple, grey, blue, and white spheres represent Co, C, N, and H atoms, respectively. **b**, Excess CH$_4$ adsorption isotherms for Co(bdp) at 25 °C with different levels of applied external mechanical pressure, indicated by the inset, colour-coded bulk powder densities, with higher densities corresponding to greater applied mechanical pressure. The maximum CH$_4$ pressure for which hysteresis is still present is indicated for each bulk density by the appropriately coloured dashed line. Filled circles represent adsorption; open circles represent desorption.

the transition to the expanded phase, lowering the overall amount of heat released compared to adsorption in the absence of a phase transition. Similarly, the transition to the collapsed phase is exothermic, and some of the heat released by the framework as it collapses should offset the endothermic desorption of CH$_4$.

In classical porous materials, low-coverage differential CH$_4$ adsorption enthalpies are generally −12 kJ mol^{-1} CH$_4$ to −15 kJ mol^{-1} CH$_4$ for adsorbents that do not have any strong CH$_4$ binding sites and are closer to −15 kJ mol^{-1} to −25 kJ mol^{-1} for adsorbents with the highest volumetric CH$_4$ capacities[7,8]. For the steepest region of the CH$_4$ adsorption isotherm of Co(bdp), the differential enthalpy is considerably lower, at just −8.4(3) kJ mol^{-1} (where the uncertainty corresponds to ±1 standard deviation), because the endothermic framework expansion partially offsets the exothermic heat of adsorption (Fig. 3c). After the transition to the expanded Co(bdp) phase is complete, the differential enthalpy approaches −13 kJ mol^{-1}, which is consistent with weak CH$_4$ physical adsorption in the absence of a phase transition to mitigate heat. To confirm the accuracy of the calculated differential enthalpies, the heat released during CH$_4$ adsorption was directly measured by performing variable-pressure microcalorimetry experiments. As shown in Fig. 3c, the differential enthalpies obtained from calorimetry are in excellent agreement with those calculated from the variable-temperature adsorption isotherms.

The total amount of heat released when increasing the pressure of CH$_4$ adsorbed in Co(bdp) from 5.8 bar to 35 bar, as would occur during refuelling of an ANG vehicle, is calculated by integrating the differential-enthalpy curve with respect to the amount of CH$_4$ adsorbed. The 73.4 kJ of heat released per litre of Co(bdp) represents a 33% reduction relative to the 109 kJ l^{-1} of heat released by HKUST-1 under the same conditions, even though the amount of CH$_4$ adsorbed in Co(bdp)

is 8% greater. We further calculate that 93.9 kJ l^{-1} of heat would be released for hypothetical CH$_4$ adsorption in a rigid Co(bdp) framework—28% higher than when adsorption occurs with a phase transition to provide heat mitigation[25].

By chemically modifying Co(bdp), we hypothesized that it might be possible to obtain a new flexible framework with a similar stepped CH$_4$ isotherm, but a higher-energy phase transition that could provide even greater intrinsic heat management. Because one-dimensional chains are known to form with tetrahedral Fe^{2+} ions bridged by μ^2-pyrazolates[26], we anticipated that it might be possible to synthesize an isostructural iron analogue of Co(bdp). By heating FeCl$_2$ and H$_2$bdp in a mixture of N,N-dimethylformamide (DMF) and methanol, we indeed obtained Fe(bdp) as yellow, block-shaped crystals. X-ray analysis of a DMF-solvated crystal (Extended Data Fig. 6) confirmed that Fe(bdp) is isostructural to Co(bdp). Fe(bdp) has a stepped high-pressure CH$_4$ isotherm at 25 °C (Fig. 1d), suggesting that this new compound also undergoes a reversible phase transition between a collapsed and expanded framework. Although the total CH$_4$ uptake is comparable to that of Co(bdp), the adsorption and desorption steps occur at the considerably higher pressures of 24 bar and 10 bar, respectively, suggesting that replacing Co with Fe increases the energy of the phase transition.

In situ powder X-ray diffraction experiments from 0 bar to 50 bar of CH$_4$ (Fig. 2b) and subsequent Rietveld refinements afforded the collapsed and CH$_4$-expanded crystal structures of Fe(bdp). Although the collapsed phase is nearly identical to that of Co(bdp), with edge-to-face π–π interactions and no accessible porosity, the volume of the expanded Fe(bdp) phase at 40 bar is 9% greater than that of Co(bdp) (Fig. 2f). In contrast to Co(bdp), we observe a second transition for Fe(bdp) at pressures above 40 bar, wherein Fe(bdp) slightly expands to a framework with nearly perfect square channels (Extended Data Fig. 6). In spite of its greater expansion and lower crystallographic density, the usable CH$_4$ capacity of Fe(bdp) is still higher than all known adsorbents at 150 v/v and 190 v/v for 35 bar and 65 bar adsorption, respectively.

Although Fe(bdp) and Co(bdp) have similar usable capacities, the initial Fe(bdp) phase transition offsets more heat, and only 64.3 kJ of heat is released per litre of adsorbent during CH$_4$ adsorption at 35 bar, which is 12% lower than for Co(bdp) and 41% lower than for HKUST-1. This is a direct consequence of the larger increase in the enthalpy of Fe(bdp) (8.1 kJ mol^{-1}) than of Co(bdp) (7.0 kJ mol^{-1}) during the phase transition, which mitigates more heat of adsorption, thereby providing a greater source of intrinsic thermal management. This result demonstrates how a slight variation in the metal–organic framework can be used to improve its intrinsic thermal management, and it is very likely that similar effects will prove possible through alteration of the bdp^{2-} bridging ligand.

Examining the temperature dependence of the CH$_4$ isotherms of Co(bdp) and Fe(bdp) (Extended Data Figs 2, 3) reveals another advantage of these materials, involving a reduction in the effect of cooling during desorption. Consistent with other gate-opening metal–organic frameworks, the CH$_4$ adsorption and desorption steps in Co(bdp) and Fe(bdp) shift to lower pressures at lower temperatures (Fig. 3a, b). As long as the temperature stays above 0 °C in Co(bdp) or −25 °C in Fe(bdp), however, the transition to the collapsed phase occurs above 5.8 bar, and the usable CH$_4$ capacity will not be affected by cooling (Supplementary Tables 2, 3). This property has practical benefits for driving in cold-weather climates and should further reduce the overall thermal management required in an ANG system.

Recent work[27−29] has shown that it is possible to induce a phase transition in flexible metal–organic frameworks by applying external mechanical pressure. With this in mind, we proposed that applying moderate mechanical pressure could provide a means of further tuning the CH$_4$ adsorption and desorption step pressures in Co(bdp) and Fe(bdp) and of increasing the energy of the phase transition to offset more heat. To investigate this concept, high-pressure CH$_4$ adsorption isotherms were measured for Co(bdp) at different levels of applied uniaxial mechanical pressure.

At higher mechanical pressures and higher compaction densities, both the adsorption and desorption isotherm steps shift to higher CH_4 pressures, which is consistent with an increase in the energy of the phase transition (Fig. 4). In addition, the isotherm hysteresis loop remains open until higher CH_4 pressures, with hysteresis observed to pressures of at least 70 bar for the highest applied mechanical pressure. Because hysteresis at a given pressure implies that a phase transition is still occurring[30], this result suggests that some Co(bdp) crystallites are expanding at much higher CH_4 pressures when under an applied external mechanical pressure. Because Co(bdp) crystallites in a bulk powder will be at different orientations with respect to the direction of uniaxial compression (Extended Data Fig. 4), there will be a distribution of local mechanical pressures experienced by different crystallites. Crystallites that experience higher external pressures will have a greater free energy change associated with the phase transition and will open at higher pressures[31]. Overall, these results present the prospect of using mechanical work, such as provided through an elastic bladder, as a means of thermal management in a gas-storage system based on a flexible adsorbent.

Designing new flexible adsorbents with stronger gas binding sites and higher-energy phase transitions provides a promising route to achieving even higher usable capacities and greater intrinsic heat management in a next generation of gas-storage materials. Moreover, improved compaction and packing strategies should allow further reductions to external thermal-management requirements and optimization of the overall storage-system performance.

1. Service, R. F. Stepping on the gas. *Science* **346,** 538–541 (2014).
2. Yeh, S. An empirical analysis on the adoption of alternative fuel vehicles: the case of natural gas vehicles. *Energy Policy* **35,** 5865–5875 (2007).
3. Whyatt, G. A. *Issues Affecting Adoption of Natural Gas Fuel in Light- and Heavy-Duty Vehicles*. Report No. PNNL-19745 (US Department of Energy, 2010).
4. Wegrzyn, J. & Gurevich, M. Adsorbent storage of natural gas. *Appl. Energy* **55,** 71–83 (1996).
5. Makal, T. A., Li, J.-R., Lu, W. & Zhou, H.-C. Methane storage in advanced porous materials. *Chem. Soc. Rev.* **41,** 7761–7779 (2012).
6. He, Y., Zhou, W., Qian, G. & Chen, B. Methane storage in metal–organic frameworks. *Chem. Soc. Rev.* **43,** 5657–5678 (2014).
7. Peng, Y. *et al.* Methane storage in metal–organic frameworks: current records, surprise findings, and challenges. *J. Am. Chem. Soc.* **135,** 11887–11894 (2013).
8. Mason, J. A., Veenstra, M. & Long, J. R. Evaluating metal–organic frameworks for natural gas storage. *Chem. Sci.* **5,** 32–51 (2014).
9. Simon, C. M. *et al.* The materials genome in action: identifying the performance limits for methane storage. *Energy Environ. Sci.* **8,** 1190–1199 (2015).
10. Advanced Research Projects Agency – Energy. *Methane Opportunities for Vehicular Energy* (Funding opportunity no. De-FOA-0000672, US Department of Energy, 2012).
11. Noguchi, H. *et al.* Clathrate-formation mediated adsorption of methane on Cu-complex crystals. *J. Phys. Chem. B* **109,** 13851–13853 (2005).
12. Horike, S., Shimomura, S. & Kitagawa, S. Soft porous crystals. *Nature Chem.* **1,** 695–704 (2009).
13. Férey, G. & Serre, C. Large breathing effects in three-dimensional porous hybrid matter: facts, analyses, rules and consequences. *Chem. Soc. Rev.* **38,** 1380–1399 (2009).
14. Schneemann, A. *et al.* Flexible metal–organic frameworks. *Chem. Soc. Rev.* **43,** 6062–6096 (2014).
15. Li, D. & Kaneko, K. Hydrogen bond-regulated microporous nature of copper complex-assembled microcrystals. *Chem. Phys. Lett.* **335,** 50–56 (2001).
16. Kitaura, R., Seki, K., Akiyama, G. & Kitagawa, S. Porous coordination-polymer crystals with gated channels specific for supercritical gases. *Angew. Chem. Int. Edn* **42,** 428–431 (2003).
17. Choi, H. J., Dincă, M. & Long, J. R. Broadly hysteretic H_2 adsorption in the microporous metal–organic framework Co(1,4-benzenedipyrazolate). *J. Am. Chem. Soc.* **130,** 7848–7850 (2008).
18. Salles, F. *et al.* Multistep N_2 breathing in the metal–organic framework Co(1,4-benzenedipyrazolate). *J. Am. Chem. Soc.* **132,** 13782–13788 (2010).
19. Hosemann, R. & Bagchi, S. N. *Direct Analysis of Diffraction by Matter* (North-Holland, 1962).
20. Sinnokrot, M. O., Valeev, E. F. & Sherrill, C. D. Estimates of the *ab initio* limits for π–π interactions: the benzene dimer. *J. Am. Chem. Soc.* **124,** 10887–10893 (2002).
21. Li, B. *et al.* A porous metal–organic framework with dynamic pyrimidine groups exhibiting record high methane storage working capacity. *J. Am. Chem. Soc.* **136,** 6207–6210 (2014).
22. Barbosa Mota, J. P., Rodrigues, A. E., Saatdjian, E. & Tondeur, D. Dynamics of natural gas adsorption storage systems employing activated carbon. *Carbon* **35,** 1259–1270 (1997).
23. Walton, K. S. & LeVan, M. D. Natural gas storage cycles: influence of nonisothermal effects and heavy alkanes. *Adsorption* **12,** 227–235 (2006).
24. Weickert, M., Marx, S., Müller, U. & Arnold, L. Sorption store for gas with multiple adsorbent media. World Intellectual Property Organization patent WO 2015/022633 A1 (2015).
25. Coudert, F.-X., Jeffroy, M., Fuchs, A. H., Boutin, A. & Mellot-Draznieks, C. Thermodynamics of guest-induced structural transitions in hybrid organic–inorganic frameworks. *J. Am. Chem. Soc.* **130,** 14294–14302 (2008).
26. Patrick, B. O., Reif, W. M., Sánchez, V., Storr, A. & Thompson, R. C. Polybis(pyrazolato)iron(II) and poly-2,2′bipyridinetetrakis(imidazolato)-diiron(II) and -dicobalt(II): from short-range magnetic interactions in the pyrazolate to long-range ferromagnetic ordering in the imidazolates. *Polyhedron* **20,** 1577–1585 (2001).
27. Beurroies, I. *et al.* Using pressure to provoke the structural transition of metal–organic frameworks. *Angew. Chem. Int. Edn* **49,** 7526–7529 (2010).
28. Yot, P. G. *et al.* Large breathing of the MOF MIL-47(V^IV) under mechanical pressure: a joint experimental–modelling exploration. *Chem. Sci.* **3,** 1100–1104 (2012).
29. Coudert, F.-X. Responsive metal–organic framework materials: under pressure, taking the heat, in the spotlight, with friends. *Chem. Mater.* **27,** 1905–1916 (2015).
30. Neimark, A. V., Coudert, F.-X., Boutin, A. & Fuchs, A. H. Stress-based model for the breathing of metal–organic frameworks. *J. Phys. Chem. Lett.* **1,** 445–449 (2010).
31. Ghysels, A. *et al.* On the thermodynamics of framework breathing: a free energy model for gas adsorption in MIL-53. *J. Phys. Chem. C* **117,** 11540–11554 (2013).

METHODS

Materials. Anhydrous *N,N*-dimethylformamide (DMF) was obtained from a JC Meyer solvent system. The ligand 1,4-benzenedipyrazole (H$_2$bdp) was synthesized according to a literature procedure[17]. All other reagents were obtained from commercial vendors and used without further purification. Ultra-high purity grade (99.999% purity) helium, dinitrogen, and methane were used for all adsorption measurements.

Synthesis of Co(bdp). The compound Co(bdp) was synthesized using a strategy adopted from a previous report[17]. Specifically, a 500-ml solvent bomb was charged with a magnetic stirring bar, Co(CF$_3$SO$_3$)$_2$ (4.96 g, 0.0139 mol), H$_2$bdp (2.46 g, 0.0117 mol), and *N,N*-diethylformamide (90 ml). The reaction mixture was degassed by the freeze–pump–thaw method for 5 cycles then sealed by closing the stopcock of the solvent bomb while the frozen reaction mixture was still under vacuum. The solvent bomb was then heated at 160 °C for 4.5 days to afford a purple microcrystalline solid. The solvent bomb was backfilled with N$_2$, and the solid was collected by filtration. Before drying, the wet solid powder was immediately transferred to a 500-ml glass jar, and 400 ml of DMF was added. The jar was heated at 120 °C for 12 h, then cooled to room temperature. The DMF was decanted and replaced with 400 ml of fresh DMF. The jar was reheated at 120 °C, followed by decanting and replacing with fresh DMF. This was repeated four additional times. The DMF was then decanted and replaced with dichloromethane (DCM). The DCM was partially decanted until 50 ml of solution was remaining. The resultant slurry was transferred to a 100-ml Schlenk flask, and the DCM was evaporated by flowing N$_2$ at room temperature. The resultant solid was dried by flowing N$_2$ at 160 °C for 12 h, then placed under dynamic vacuum at 160 °C for 24 h. The activated solid was immediately transferred to a glovebox and handled under a N$_2$ atmosphere for all further experiments.

Synthesis of Fe(bdp). In a glovebox under a N$_2$ atmosphere, H$_2$bdp (0.200 g, 0.95 mmol) in DMF (9 ml) was heated to 120 °C while stirring for 20 min in a 20 ml glass vial. The resultant yellow suspension was cooled. A solution of FeCl$_2$ (0.197 g, 1.55 mmol) in methanol (1 ml) was added to the cooled suspension of H$_2$bdp in DMF, and the vial was sealed and heated at 120 °C while stirring. The hot, orange–yellow solution yielded a yellow microcrystalline powder after several hours. Samples suitable for gas adsorption studies were prepared using multiple vials of the same reaction scale in a glovebox under a N$_2$ atmosphere and by washing the resultant material nine times with hot DMF (9 × 18 ml), before drying under high vacuum at 170 °C for 24 h. The activated sample was handled under a N$_2$ atmosphere for all further experiments. IR (neat, cm^{-1}): 1,573 (s), 1,336 (w), 1,239 (s), 1,110 (s), 1,041 (s), 952 (s), 859 (s), 849 (s), 832 (s), 824 (s), 644 (s), 534 (s). Anal. Calcd for FeC$_{12}$H$_8$N$_4$: C, 54.58; H, 3.05; N, 21.22. Found: C, 54.18; H, 2.36; N, 20.67. To obtain single crystals suitable for X-ray diffraction, a 9:1 mixture of DMF and methanol was used to create solutions of FeCl$_2$ (9.0 mg, 0.07 mmol in 0.1 ml solvent) and H$_2$bdp (4.0 mg, 0.019 mmol in 0.9 ml solvent). The FeCl$_2$ solution and the H$_2$bdp solution were added together in a 4-ml vial. The vial was then sealed, and the clear yellow solution was heated at 120 °C for 24 h. Block-shaped yellow crystals formed on the sides of the vial after several hours.

Low-pressure gas adsorption measurements. Gas adsorption isotherms for pressures in the range of 0–1.1 bar were measured using a Micromeritics ASAP 2020 or 2420 instrument. Activated samples were transferred under a N$_2$ atmosphere to preweighed analysis tubes, which were capped with a Transeal. Each sample was evacuated on the ASAP until the outgas rate was less than 3 μbar min^{-1}. The evacuated analysis tube containing degassed sample was then carefully transferred to an electronic balance and weighed to determine the mass of sample (typically 100–200 mg). The tube was then fitted with an isothermal jacket and transferred back to the analysis port of the ASAP. The outgas rate was again confirmed to be less than 3 μbar min^{-1}. Langmuir surface areas were determined by measuring N$_2$ adsorption isotherms in a 77-K liquid N$_2$ bath and calculated using the Micromeritics software, assuming a value of 16.2 Å^2 for the molecular cross-sectional area of N$_2$. The Langmuir surface areas of Co(bdp) and Fe(bdp) are 2,911 m^2 g^{-1} and 2,780 m^2 g^{-1}, respectively. Full 77-K N$_2$ adsorption isotherms for Co(bdp) and Fe(bdp) can be found in Supplementary Fig. 1. Note that BET surface areas cannot be accurately determined for either framework because of the steps in the low-pressure region of the 77-K N$_2$ adsorption isotherms.

High-pressure CH$_4$ adsorption measurements. High-pressure CH$_4$ adsorption isotherms in the range of 0–70 bar were measured on an HPVA-II-100 from Particulate Systems, a Micromeritics company. In a typical measurement, 0.5–1.0 g of activated sample was loaded into a tared stainless steel sample holder inside a glovebox under a N$_2$ atmosphere. Prior to connecting the sample holder to the VCR fittings of the complete high-pressure assembly inside the glovebox, the sample holder was weighed to determine the sample mass. The sample holder was then transferred to the HPVA-II-100, connected to the instrument's analysis port via an OCR fitting, and evacuated at room temperature for at least 2 h. The

sample holder was placed inside an aluminium recirculating Dewar connected to a Julabo FP89-HL isothermal bath filled with Julabo Thermal C2 fluid. The temperature stability of the isothermal bath is ±0.02 °C. Methods for accurately measuring the relevant sample freespaces, which involve the expansion of He from a calibrated volume at 0.7 bar and 25 °C to the evacuated sample holder, were described in detail previously[8]. Non-ideality corrections were performed using the CH$_4$ compressibility factors tabulated in the NIST REFPROP database[32] at each measured temperature and pressure.

A sample size of 1.032 g was used for the 25-°C usable capacity calculations, compaction studies, and cycling studies with Co(bdp), whereas a sample size of 0.584 g was used for the variable-temperature measurements. For Fe(bdp), a sample size of 0.274 g was used for high-pressure adsorption measurements, with the exception of the isotherms measured at −12 °C and −25 °C for which a sample size of 0.322 g was used.

To determine the usable CH$_4$ capacity of Co(bdp) and Fe(bdp), experimentally measured excess gravimetric adsorption data (Extended Data Fig. 3) were converted to total volumetric adsorption data using the pore volume and crystallographic density of the CH$_4$-expanded phases (see Supplementary Text for details). All usable capacity calculations assume a minimum desorption pressure of 5.8 bar. Although the minimum desorption pressure required for natural gas to flow from the adsorbent to the combustion engine can vary from 3.5 bar to 10 bar depending on the specific requirements of fuel injectors, filters, and other engine components, a value of 5.8 bar has been adopted by many groups[9,10] for initial materials comparisons.

High-pressure CH$_4$ adsorption measurements under applied mechanical pressure. For the high-pressure CH$_4$ adsorption measurements of Co(bdp) at different applied mechanical pressures, an aluminium sample holder was designed and used (Extended Data Fig. 5). The sample is loaded in the volume between the fritted and blank gaskets. The free volume between the fritted and blank gaskets in the absence of a sample was determined by expansion of He from a calibrated volume to be 5.242 ml. Initially, 1.032 g of Co(bdp) was loaded into this volume, resulting in a bulk density of 0.197 g ml^{-1} for the uncompacted powder. After measuring a high-pressure CH$_4$ adsorption isotherm, the sample holder was returned to a glovebox under a N$_2$ atmosphere, and the cell was opened by removing the cap behind the blank gasket. An aluminium rod with an outer diameter slightly less than the inner diameter of the sample holder was then inserted. A mechanical press was used to compact the sample by pushing down on the rod. A fresh blank gasket was then sealed behind the rod so that the rod was left pressed against the sample, with a continuously applied uniaxial mechanical pressure. The sample holder was returned to the high-pressure instrument and fully evacuated before measuring a high-pressure CH$_4$ adsorption isotherm. This experiment was repeated after inserting additional metal rods to further compact the Co(bdp), increase the applied mechanical pressure, and reduce the sample volume. Packing densities for each experiment were calculated by subtracting the volume of each rod from the original sample volume.

The decrease in the total amount of CH$_4$ adsorbed at higher mechanical pressures (Fig. 4) is not due to framework degradation, as is often observed when compacting classical adsorbents[7], and can instead be explained by insufficient CH$_4$ pressure to induce a phase transition in some crystallites and by a lack of sufficient free volume for all crystallites to expand into. To confirm this, a CH$_4$ adsorption isotherm was measured after compacting collapsed Co(bdp) to a packing density of 0.75 g cm^{-3}, which is just below the crystallographic density of the expanded phase, and releasing the applied mechanical pressure by removing the metal rod. The resulting isotherm was found to be nearly identical to the pre-compaction isotherm, demonstrating that all Co(bdp) crystallites could once again fully expand (Extended Data Fig. 5).

Powder X-ray diffraction measurements. Powder X-ray diffraction data for Co(bdp) and Fe(bdp) were collected on beamline 17-BM-B at the Advanced Photon Source (APS) at Argonne National Laboratory and beamline MS-X04SA at the Swiss Light Source (SLS) at the Paul Scherrer Institut (Extended Data Fig. 7). For variable CH$_4$ pressure experiments, approximately 10 mg of fully desolvated framework was loaded into 1.5-mm quartz glass capillaries inside a glovebox under a N$_2$ atmosphere. Each capillary was attached to a custom-designed gas-dosing cell, which is equipped with a gas valve, and was then transferred to the goniometer head. All adsorbed N$_2$ was removed by evacuating *in situ* using a turbomolecular pump. A cryostat was used to hold the temperature constant at 25 °C, and variable pressures of CH$_4$ were dosed to the samples. Diffraction data were collected after allowing each dose to equilibrate for several minutes. All X-ray wavelengths were between 0.72 Å and 0.78 Å, and are specified for each experiment in the relevant figures and tables.

The structure solution and refinement procedure used in this study followed the standard protocol developed by us, and others, for the structural characterization

of polycrystalline samples of non-ideal crystallinity and moderately complex structures by *ab initio* powder diffraction methods. The specific details of the crystal structure determinations are discussed in the Supplementary Information, but the general procedure, which was fully adopted for the collapsed Co(bdp) phase, is summarized here. A standard peak search, followed by peak profile fitting was first used to determine accurate peak positions of several well-separated low-angle peaks. These peak positions were used to obtain approximate lattice parameters via the single-value-decomposition indexing procedure implemented in the software TOPAS-R (Bruker AXS, version 3.0, 2005), which were later refined by the structureless Le Bail method as implemented in TOPAS-R. Systematic absences, density considerations and previous knowledge of isotypic species coherently allowed the derivation of the correct space group, which was later confirmed by successful structure solution and Rietveld refinement. The structural model was derived using the simulated annealing procedure as implemented in TOPAS-R, which is a real-space structure-solution technique, with a single freely floating metal ion and an idealized half bdp^{2-} ligand defined using z-matrix formalism. In the collapsed phase of Co(bdp), for instance, the metal atom was located on a two-fold axis at $(0, y, 1/4)$, whereas the half bdp^{2-} ligand was hinged about the inversion centre at $(1/4, 3/4, 0)$. Once an initial structural model was established, complete Rietveld refinements were performed in the software TOPAS-R. The background was modelled with Chebyshev polynomials, and Lorentz and absorption correction factors were applied. A single isotropic B value was attributed to all atoms, and found to act, as expected, as a scavenger for θ-dependent systematic errors, which are not suitably taken into account in the data-reduction process. After the retrieval of the lattice metrics and space-group symmetry for the CH_4-expanded phases, defining a starting structural model was straightforward, because it is implicit in the isotypic nature of the compounds. The contribution of the (probably tumbling, but not necessarily randomly located) CH_4 molecules to the overall scattering power was neglected, which probably contributes to the decreased physical meaning of the atomic displacement parameter values, as is common for crystal structures determined from powder diffraction data.

As indicated in the main text, the peak widths of the collapsed Co(bdp) and Fe(bdp) could not be modelled by convoluting conventional Lorentzian and Gaussian functions (or their combinations) with systematic $1/\cos(\theta)$ or $\tan(\theta)$ dependency, respectively, or with smooth hkl-dependent models (such as spherical harmonics). Instead, we began by separately modelling the hkl peak widths as distinct from the axial reflections of the $h00$- and $0k0$-type peak widths using a purely phenomenological model. We also developed a paracrystalline model for collapsed Co(bdp) (discussed in Supplementary Text) that is also representative of the collapsed Fe(bdp) phase.

Single-crystal X-ray diffraction measurements. X-ray diffraction analyses were performed on a single crystal of Fe(bdp) that was coated with Paratone-N oil and mounted on a MiTeGen loop. The crystal of Fe(bdp) was first kept frozen at 100 K by an Oxford Cryosystems Cryostream 800 plus, and after a full data collection, the crystal was warmed to 298 K for a second data collection. Diffraction data for Fe(bdp) was collected at beamline 11.3.1 at the Advanced Light Source, Lawrence Berkeley National Laboratory using synchrotron radiation (wavelength $\lambda = 0.7749$ Å) with 1° omega scans for the 100-K structure, and 4° phi and 1° omega scans for the 298 K structure. A Bruker PHOTON100 CMOS diffractometer was used for data collection, and the corresponding Bruker AXS APEX II software was used for data collection and reduction. Raw data were integrated and corrected for Lorentz and polarization effects using the Bruker AXS SAINT software. Absorption corrections were applied using TWINABS for the 100-K structure and SADABS for the 298-K structure. Space-group assignments were determined by examination of systematic absences, E statistics, and successive refinement of the structures of Fe(bdp) at 100 K and 298 K. The structures were solved using direct methods with SHELXS and refined using SHELXL operated in the OLEX2 interface. Thermal parameters were refined anisotropically for all non-hydrogen atoms. Hydrogen atoms were placed in ideal positions and refined using a riding model for all structures.

The crystal was determined to be twinned at 100 K and a suitable unit cell was determined that is similar to that previously reported for Co(bdp)•3DMF in the space group $P2_1/c$ (ref. 33). The program CELL_NOW was used to determine the orientation matrices, and the domains were found to related by a 179.9° rotation around the reciprocal axis [0.5, 0, 1]. Raw data for both matrices were integrated and corrected for absorption using TWINABS. Solution and refinement of the data in $P2_1/c$ required substantially fewer restraints in structure refinement and gave much lower values for R_1 compared to those solved in other space groups. Solvent molecules could be refined anisotropically in the crystal of Fe(bdp) at 100 K, accounting for all pore void space.

When the crystal was warmed to 298 K, the space group was determined to be $C222_1$ instead of $P2_1/c$ and was refined as an inversion twin (batch scale factor, BASF = 0.52(4); the uncertainty corresponds to ± 1 s.d.). At 298 K, there was extensive solvent disorder that could not be modelled. A solvent mask was applied, as implemented in OLEX2, to account for unassigned electron density within the pores. The loss in intensity of spots upon warming to 298 K, and the large anisotropic displacement parameters that result from linker and solvent disorder, gave rise to A- and B-level alerts from checkCIF (http://checkcif.iucr.org). Responses addressing these alerts have been included in the CIF (crystallographic information file, available from the Cambridge Crystallographic Data Centre; see Author Information) and can be read in reports generated by checkCIF.

Scanning electron microscopy. Scanning electron microscopy (SEM) samples of Co(bdp) and Fe(bdp) were prepared by dispersing microcrystalline powders into DCM and drop casting onto a silicon chip (Extended Data Fig. 4). To dissipate charge, the samples were sputter coated with approximately 3 nm of Au (Denton Vacuum). Crystals were imaged at 5 keV and 12 μA by field emission SEM (JEOL FSM6430).

Microcalorimetry measurements. Approximately 0.2 g of Co(bdp) was used for combined microcalorimetry and high-pressure CH_4 adsorption experiments. Before each experiment, samples were outgassed *ex situ* at 423 K for 16 h under a dynamic vacuum of 10^{-3} mbar. The microcalorimetry experiments were performed using a custom-built manometric adsorption apparatus coupled with a Tian–Calvet-type microcalorimeter[34]. This experimental device allows the simultaneous determination of the adsorption isotherm and the adsorption enthalpy using a point-by-point introduction of gas to the sample. A multi-pneumovalve system allows the introduction of the adsorbate to the sample. An exothermic thermal effect accompanied each introduction, which is due to both the adsorption process and gas compression. This peak in the energy curve with time is thus integrated to calculate a pseudo-differential enthalpy of adsorption for each dose. Errors in this calculation can be estimated at ± 1 kJ mol^{-1}. Experiments were carried out at 303 K and up to 70 bar with CH_4 of a purity of above 99.999%.

32. Lemmon, E. W., Huber, M. L. & McLinden, M. O. *NIST Standard Reference Database 23: Reference Fluid Thermodynamic and Transport Properties—REFPROP Version 8.0* (National Institute of Standards and Technology, 2007).
33. Lu, Y. *et al.* A cobalt(II)-containing metal-organic framework showing catalytic activity in oxidation reactions. *Z. Anorg. Allg. Chem.* **634,** 2411–2417 (2008).
34. Llewellyn, P. L. & Maurin, G. Gas adsorption microcalorimetry and modeling to characterise zeolites and related materials. *C. R. Chimie* **8,** 283–302 (2005).
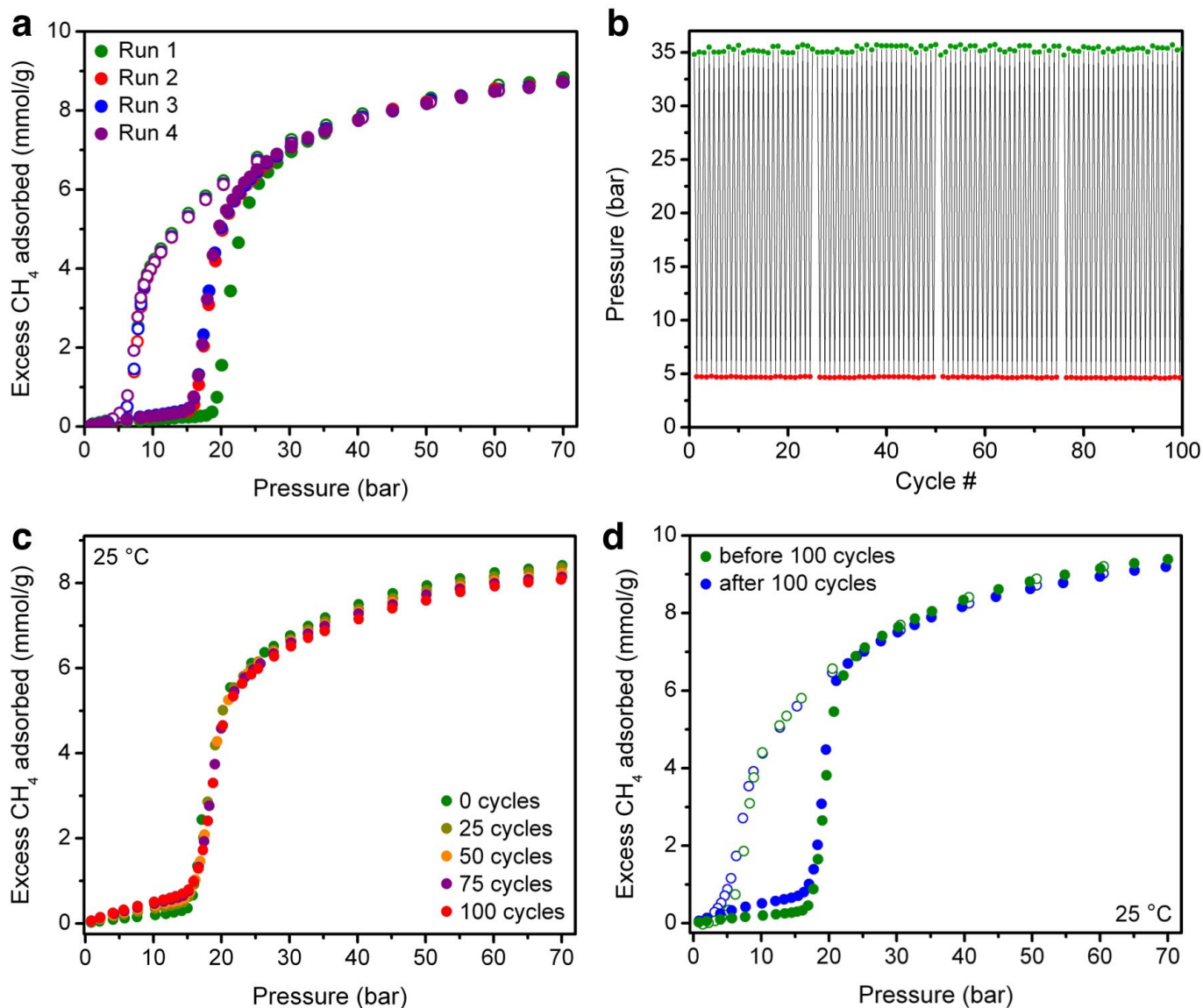
Extended Data Figure 1 | High-pressure CH$_4$ cycling. a, Excess CH$_4$ isotherms at 25 °C for Co(bdp) repeated four times on the same sample, which was regenerated under vacuum at 25 °C for 2 h between measurements. The adsorption step is at a slightly higher pressure during the first run because there is probably a slightly higher energy barrier to the first expansion of a freshly packed sample; however, the desorption steps occur at identical pressures for all four runs. **b**, The adsorption and desorption pressures are shown as green and red circles, respectively, for 100 CH$_4$ adsorption–desorption cycles in Co(bdp) at 25 °C. **c**, Excess CH$_4$ adsorption isotherms at 25 °C for Co(bdp) after 0, 25, 50, 75, and 100 cycles of 35-bar adsorption and 5-bar desorption. **d**, Excess CH$_4$ isotherms at 25 °C for Co(bdp) before (green) and after (blue) the 100 adsorption–desorption cycles between 35 bar and 5 bar. Filled and open circles in **a** and **d** correspond to adsorption and desorption, respectively.
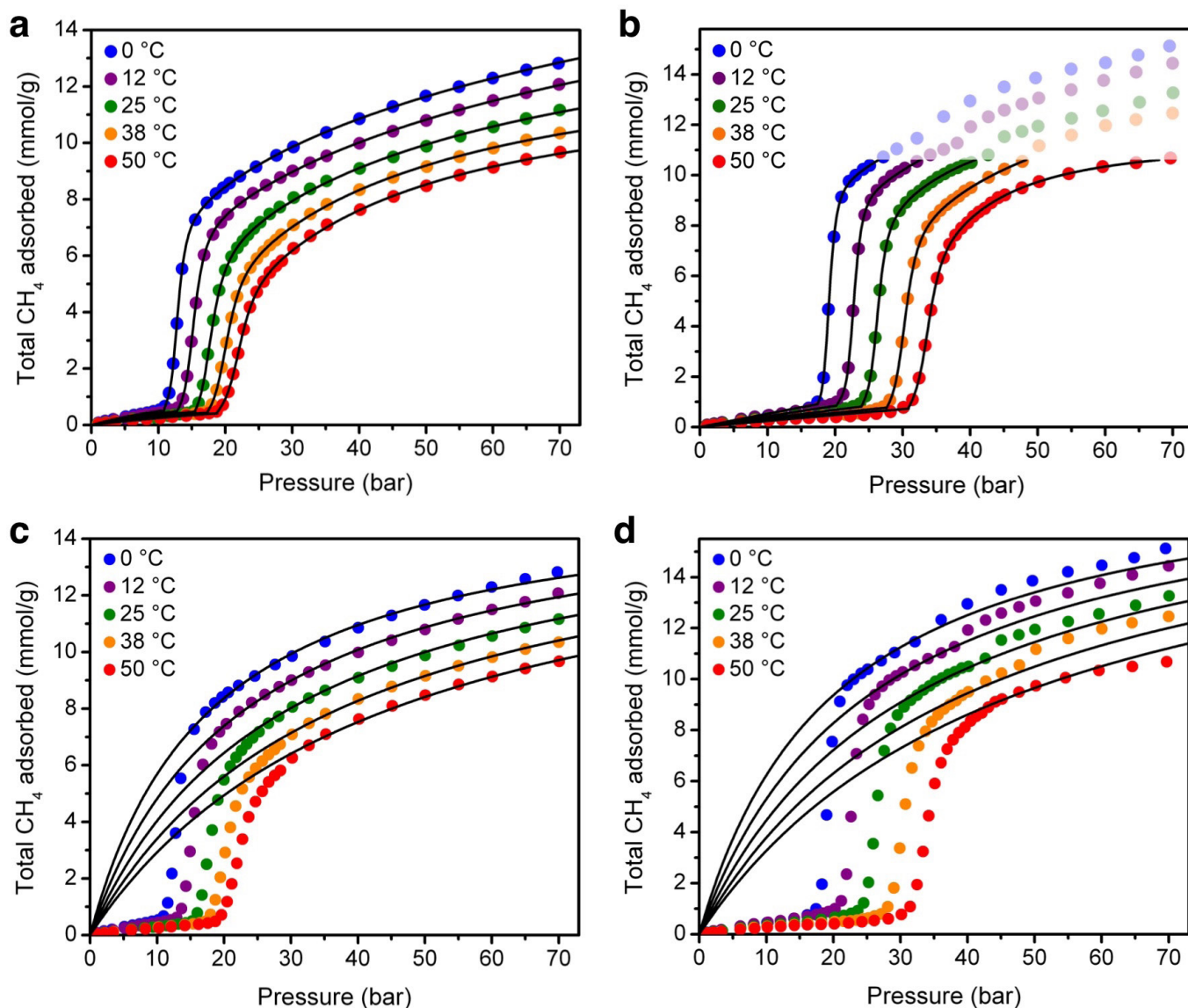
Extended Data Figure 2 | Adsorption isotherm fitting. a, Total CH_4 adsorption isotherms at 0 °C, 12 °C, 25 °C, 38 °C, and 50 °C for Co(bdp), with adsorption after the step fitted independently at each temperature with an offset dual-site Langmuir–Freundlich equation. The small pre-step adsorption was fitted with a single-site Langmuir model. **b**, Total CH_4 adsorption isotherms at 0 °C, 12 °C, 25 °C, 38 °C, and 50 °C for Fe(bdp) with adsorption after the phase transition fitted independently at each temperature with an offset dual-site Langmuir–Freundlich equation. The pre-step adsorption was fitted with a single-site Langmuir model, and the isotherms were only fitted to a maximum loading of 10.6 mmol g^{-1}, as indicated by the shading, to avoid complications from the second transition at higher CH_4 loadings. As such, differential enthalpies are only calculated up to a maximum loading of 10.6 mmol g^{-1}. **c**, Total CH_4 adsorption isotherms at 0 °C, 12 °C, 25 °C, 38 °C, and 50 °C for Co(bdp) with the corresponding single-site Langmuir fit for CH_4 adsorption in the expanded phase. **d**, Total CH_4 adsorption isotherms at 0 °C, 12 °C, 25 °C, 38 °C, and 50 °C for Fe(bdp) with the corresponding single-site Langmuir fit for CH_4 adsorption in the 40-bar expanded phase. The data were only fitted for the region of the isotherms that falls after the initial hysteresis loop closes and before the second isotherm step. All single- and dual-site Langmuir–Freundlich fits are shown as black lines.
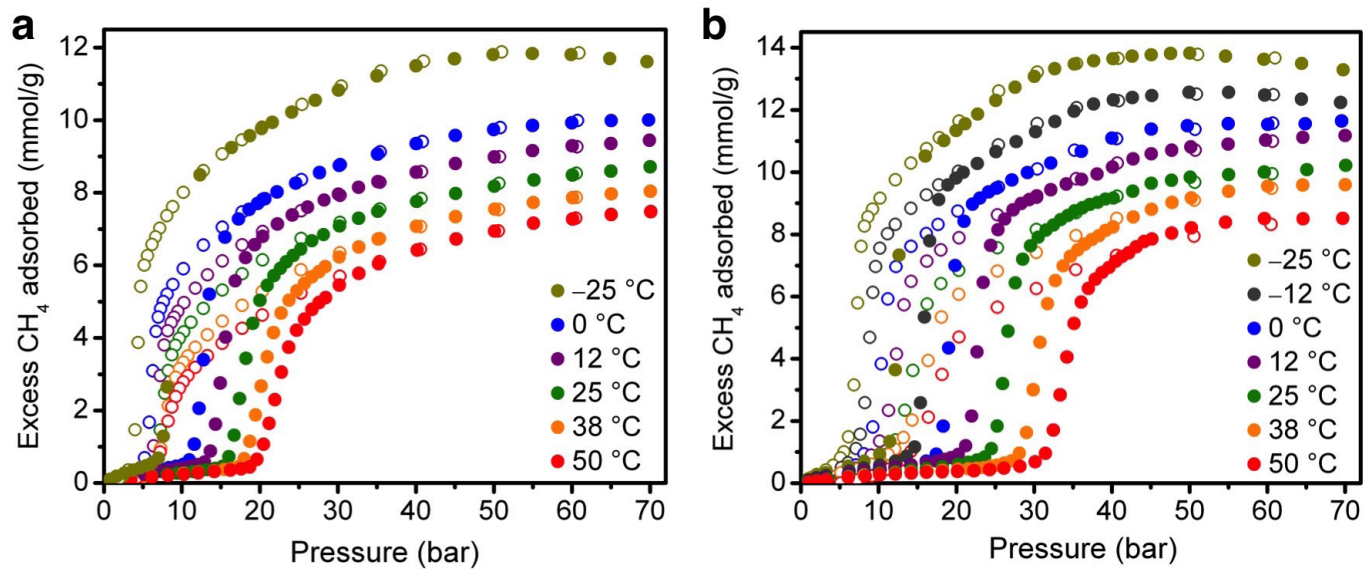
Extended Data Figure 3 | Excess CH₄ adsorption data. a, Excess CH_4 adsorption isotherms at $-25\,°C$, $0\,°C$, $12\,°C$, $25\,°C$, $38\,°C$, and $50\,°C$ for Co(bdp).
b, Excess CH_4 adsorption isotherms at $-25\,°C$, $-12\,°C$, $0\,°C$, $12\,°C$, $25\,°C$, $38\,°C$, and $50\,°C$ for Fe(bdp). Filled and open circles correspond to adsorption and desorption, respectively.

a

b

c
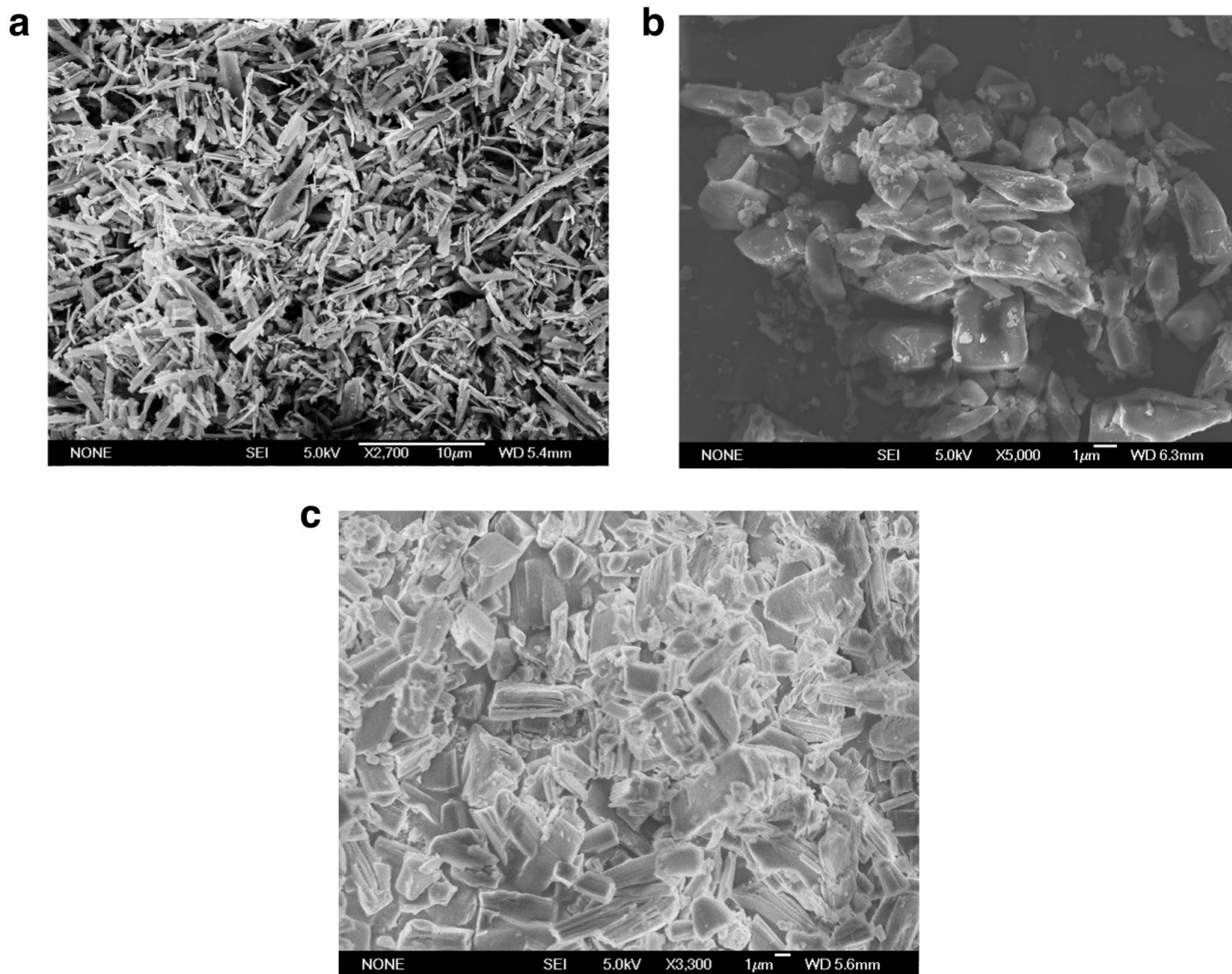
Extended Data Figure 4 | SEM images. a, SEM image of DMF-solvated Co(bdp) microcrystalline powder. Scale bar, 10 μm. **b**, SEM image of Co(bdp) microcrystalline powder after more than 100 CH_4 adsorption–desorption cycles. Scale bar, 1 μm. **c**, SEM image of desolvated Fe(bdp) microcrystalline powder. Scale bar, 1 μm.

a

b
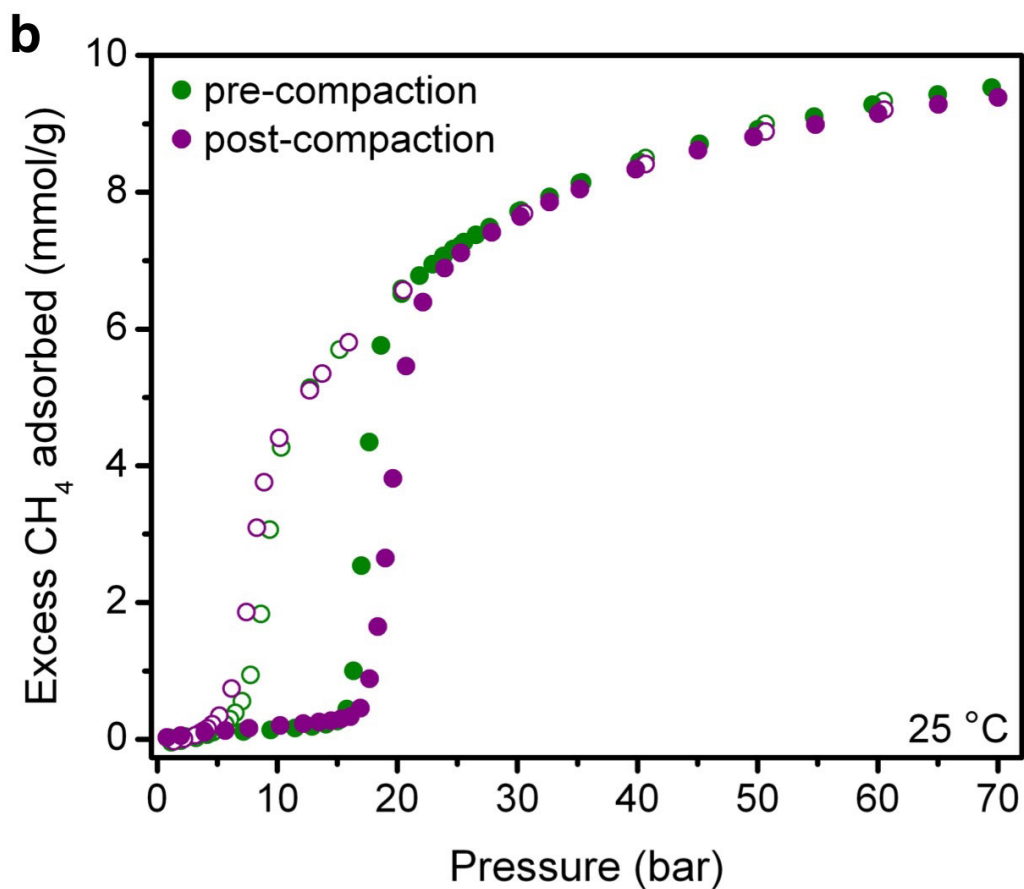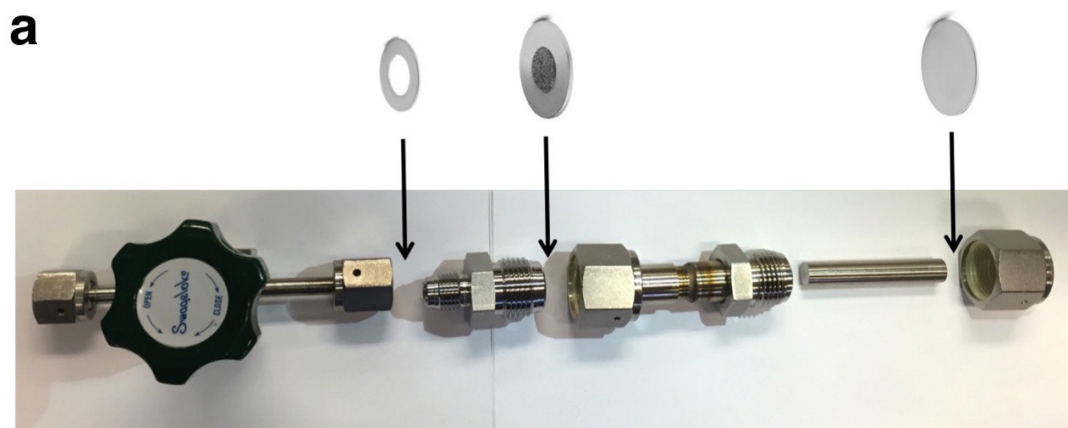
Extended Data Figure 5 | Effect of mechanical pressure. a, Sample holder used for combined applied mechanical pressure and high-pressure CH$_4$ adsorption experiments. The sample is located in the volume to the right of the fritted gasket and to the left of the blank gasket. A press is used to compact metal rods of different lengths against the sample, and the blank gasket is sealed behind the rod so that the uniaxial applied mechanical pressure (and constricted volume) is maintained throughout the high-pressure CH$_4$ adsorption experiment. **b**, Excess CH$_4$ isotherms at 25 °C for Co(bdp) before (green) and after (purple) the applied mechanical pressure studies. Filled and open circles correspond to adsorption and desorption, respectively.
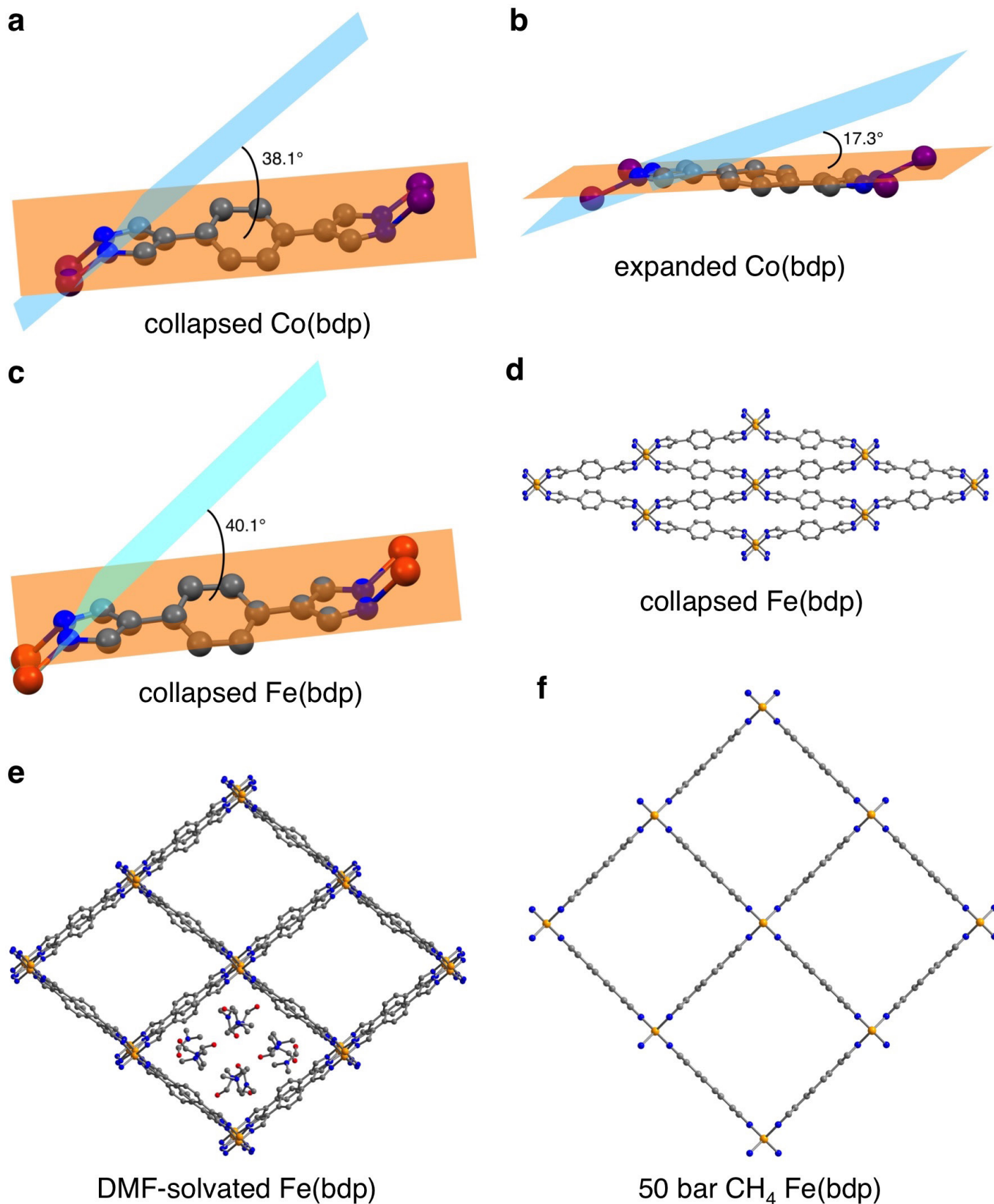
Extended Data Figure 6 | Solid-state structures. a, b, The angles between the plane of the pyrazolate (light orange) and the Co–N–N–Co plane (light blue) are 38.1° and 17.3° in the collapsed and the CH_4-expanded phases of Co(bdp), respectively. **c,** The angle between the plane of the pyrazolate (light orange) and the Fe–N–N–Fe plane (light blue) is 40.1° in the collapsed phase of Fe(bdp). **d,** Structure of the collapsed phase of Fe(bdp) under vacuum at 25 °C. **e,** Structure of the DMF-solvated phase of Fe(bdp) at 100 K. **f,** Idealized average structure of the 50-bar CH_4-expanded phase of Fe(bdp) at 25 °C. In **a–f,** Grey, blue, red, purple, and orange spheres represent C, N, O, Co, and Fe atoms, respectively; H atoms are omitted for clarity.
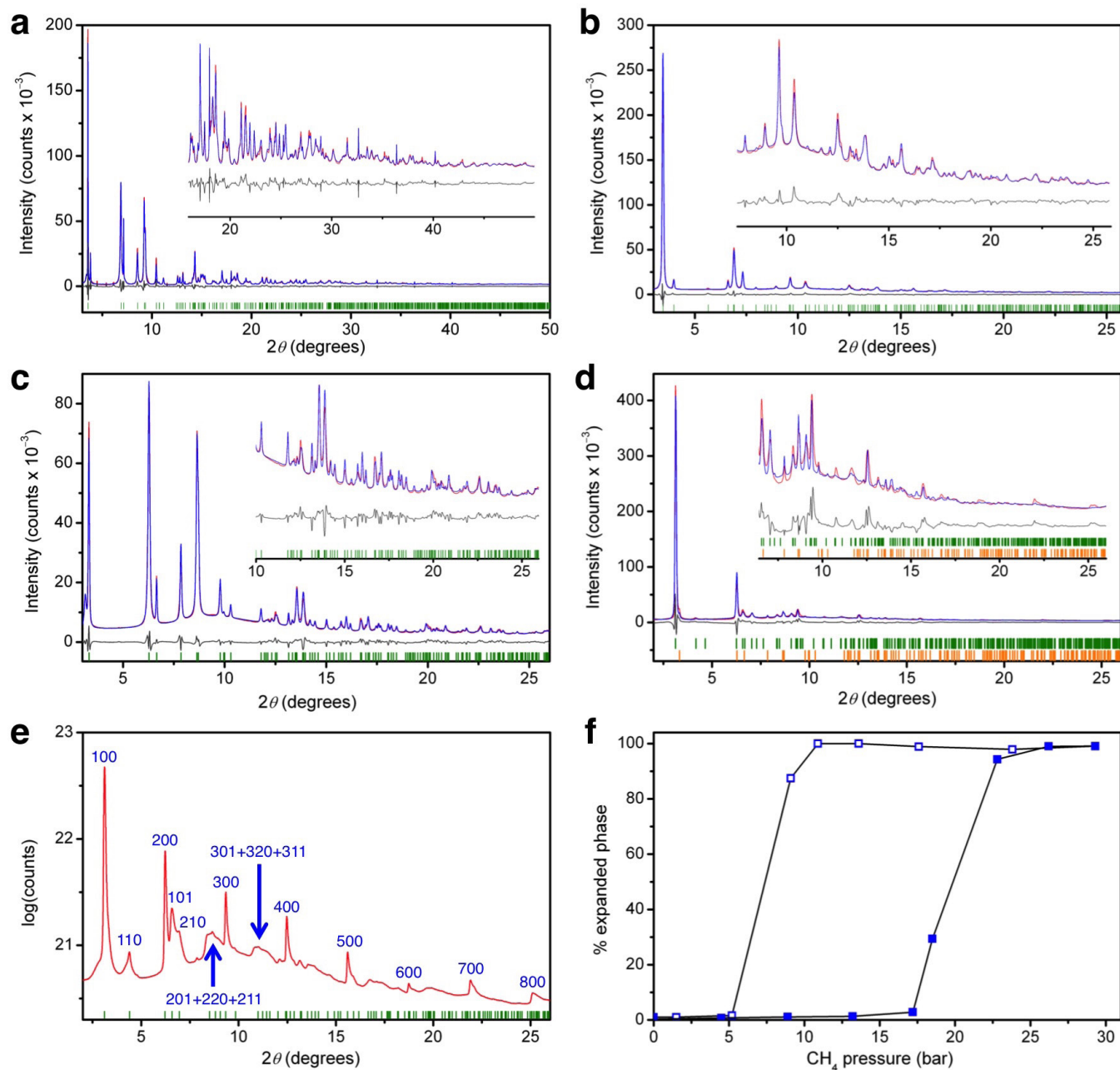
Extended Data Figure 7 | Powder X-ray diffraction. a–d, Rietveld refinements for powder X-ray diffraction data (2θ is the diffraction angle) for Co(bdp) at 25 °C and under vacuum with $\lambda = 0.77475$ Å (**a**), for Co(bdp) at 30 bar of CH_4 and 25 °C with $\lambda = 0.75009$ Å (**b**), for Fe(bdp) under vacuum at 25 °C with $\lambda = 0.72768$ Å (**c**), and for Fe(bdp) at 40 bar of CH_4 and 25 °C with $\lambda = 0.72768$ Å (**d**). Red and blue lines represent the observed and calculated diffraction patterns, respectively. Grey lines represent the difference between observed and calculated patterns, and green and orange tick marks indicate calculated Bragg peak positions. The broad hump observed at 10° in the diffraction patterns is due to diffuse

scattering from the sample holder (a thick-walled quartz glass capillary). The insets are magnified views of the main plots. **e**, Powder X-ray diffraction data for Fe(bdp) at 50 bar of CH_4 and 25 °C ($\lambda = 0.72768$ Å). Green tick marks indicate Bragg angles for space-group-permitted reflections; the corresponding Miller indices are indicated for the most prominent peaks. Blue arrows indicate broad humps where multiple reflections overlap. **f**, The percentage of the expanded phase of Co(bdp) that is present in the variable-pressure experimental powder X-ray diffraction patterns as a function of CH_4 pressure. The filled squares represent data collected during adsorption; the open squares represent data collected during desorption.
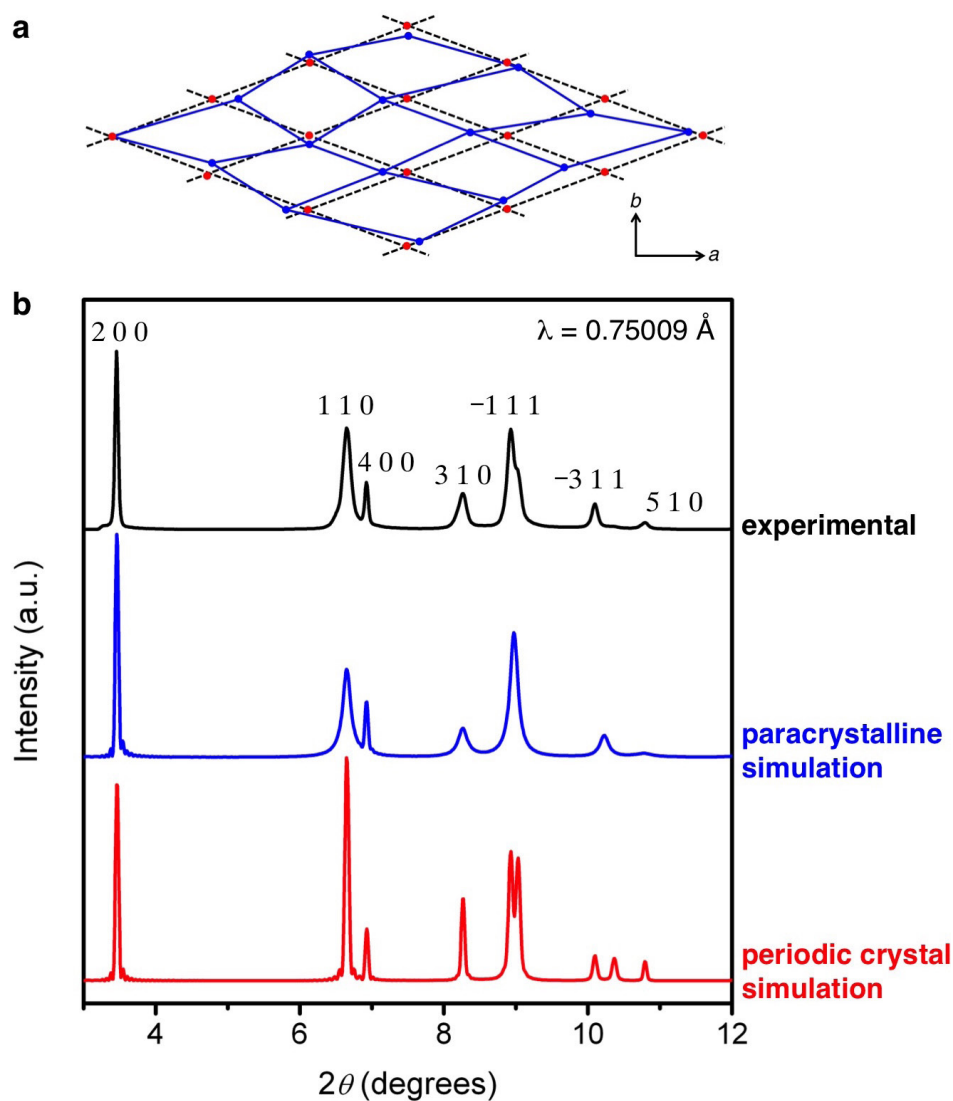
Extended Data Figure 8 | Paracrystalline model. a, An illustration of the paracrystalline distortion in the crystallographic *a*–*b* plane of the collapsed phases of Co(bdp) and Fe(bdp) that leads to complex Bragg peak broadening. Black dashed lines represent the periodic crystal lattice; blue lines represent the paracrystal. Red circles represent the positions of metal–pyrazolate chains in the periodic lattice; blue circles represent their positions in a paracrystal. The magnitude of the paracrystalline distortion has been exaggerated for clarity. **b**, Simulated diffraction patterns are shown for a periodic collapsed Co(bdp) nanocrystal (75 nm × 60 nm × 43 nm; red trace) and for a paracrystal of equivalent size (blue trace). The upper trace (black) corresponds to the background-subtracted experimental diffraction pattern of the collapsed phase of Co(bdp) at 25 °C; the corresponding Miller indices are indicated for the most prominent peaks. For clarity, the three patterns have been given an arbitrary *y* offset; a.u., arbitrary units. Similar anisotropic peak broadening, which inflates *hk*0 peaks (but not *h*00 or 0*k*0 ones), is clearly visible in the experimental diffraction pattern and the paracrystalline simulation. The exact full-widths at half-maximum for the experimental and simulated Bragg peaks are given in Supplementary Table 16.